

OPEN

A new biocompatible ternary Layered Double Hydroxide Adsorbent for ultrafast removal of anionic organic dyes

Garima Rathee¹, Amardeep Awasthi¹, Damini Sood¹, Ravi Tomar¹, Vartika Tomar¹ & Ramesh Chandra^{1,2*}

It would be of great significance to introduce a new biocompatible Layered Double Hydroxide (LDH) for the efficient remediation of wastewater. Herein, we designed a facile, biocompatible and environmental friendly layered double hydroxide (LDH) of NiFeTi for the very first time by the hydrothermal route. The materialization of NiFeTi LDH was confirmed by FTIR, XRD and Raman studies. BET results revealed the high surface area (106 m²/g) and the morphological studies (FESEM and TEM) portrayed the sheets-like structure of NiFeTi nanoparticles. The material so obtained was employed as an efficient adsorbent for the removal of organic dyes from synthetic waste water. The dye removal study showed >96% efficiency for the removal of methyl orange, congo red, methyl blue and orange G, which revealed the superiority of material for decontamination of waste water. The maximum removal (90%) of dyes was attained within 2 min of initiation of the adsorption process which supported the ultrafast removal efficiency. This ultrafast removal efficiency was attributed to high surface area and large concentration of -OH and CO₃²⁻ groups present in NiFeTi LDH. In addition, the reusability was also performed up to three cycles with 96, 90 and 88% efficiency for methyl orange. Furthermore, the biocompatibility test on MHS cell lines were also carried which revealed the non-toxic nature of NiFeTi LDH at lower concentration (100% cell viability at 15.6 µg/ml). Overall, we offer a facile surfactant free method for the synthesis of NiFeTi LDH which is efficient for decontamination of anionic dyes from water and also non-toxic.

The organic dye contaminants released from various sources are one of the major global environmental issues¹. The organic water-soluble dyes can be classified as anionic, cationic and non-ionic dyes². Most of these dyes have been reported to be mutagenic, toxic and cancer causing in nature³. Unfortunately, 7 × 10⁵ tons of dye contaminants are released into water every year which has posed a threat to aquatic life by reducing the penetration of light and visibility through the water surface. This has a direct consequence on the photosynthetic cycle⁴.

To study the effect of dyes on the ecosystem a number of studies are performed for example the effects of five azo food dyes (tartrazine, carmoisine, sunset yellow, ponceau 4R and allura red) on the *in vitro* synthesis of leukotriene B₄ and F₂-isoprostanates and suggested their high potency to promote pro-inflammatory responses⁵. Oliveria *et al.* used ecotoxicity testing battery to study the genotoxicity and acute toxicity of various dyes on different tropic levels. They landed up with the conclusion that Direct Black 38 and Reactive Blue 15 dyes causes acute toxicity and genotoxicity among aquatic organisms. However, Direct Black 38 was considered to be most toxic dye because of its lethal toxicity and tendency for DNA damage⁶. Further, molecular docking and multispectroscopy studies were also carried out by Naveenraj *et al.* to study the interaction of Acid Orange 10 with Bovine Serum Albumin (BSA) and Human Serum Albumin (HSA) and therefore, revealed the toxic effects of Acid Orange 10 during blood transportation process⁷. As a consequence, the need of the hour is to develop an effective technique for the removal of dye contaminants from wastewater.

Various techniques like biological treatment⁸, coagulation⁹, ozonation¹⁰, membrane filtration¹¹, chemical oxidation¹², ion exchange methods¹³, photocatalysis^{14,15} and adsorption¹⁶ have been widely used for dye removal

¹Drug Discovery & Development Laboratory, Department of Chemistry, University of Delhi, Delhi, 110007, India. ²Dr. B. R. Ambedkar Centre for Biomedical Research University of Delhi, Delhi, 110007, India. *email: rameshchandragroup@gmail.com

Adsorbent	Dye implemented	% Removal (approx.)	Contact time (approx.)	pH	Reference
MgAl-LDH supported Cu-(BDC) MOF	Methyl orange	99	20 min	6	⁴⁰
Ni ₄ Fe ₁ -CO ₃ -LDH	Methyl orange	20	120 min	5–6	⁴¹
ZnAl-LDH/Al(OH) ₃	Methyl Orange	98	50 min	4	⁴²
ZnAl-LDH/Al(OH) ₃	Congo Red	99	200 min	6	⁴²
S/NiFe-LDH (1:1),	Methyl Orange	82.6	30 min	3	⁴³
S/NiFe-LDH (2:1)	Methyl Orange	63.2	60 min	3	⁴³
Mg–Al–CO ₃ LDH– carbon dot composites	Methyl blue	96	20 min	9.45	⁴⁴
C/MnCuAl LDOs	Congo Red	Attained equilibrium (58%)	180 min	4.5	⁴⁵
Ca-Al-LDHs	Congo Red	Attained equilibrium	80 min	7	⁴⁶
Ni/Fe/Ti LDH Ni/Fe/Ti LDH	Methyl Orange	>95%	4 min	7–8	In this study
	Congo Red	>95%	6 min	5–12	In this study
Ni/Fe/Ti LDH	Methyl blue	>95%	1 min	5–12	In this study
Ni/Fe/Ti LDH	Orange G	>95%	4 min	7–8	In this study

Table 1. Reported adsorbents for dye removal and their parameters.

but they suffer various limitations. Among all the techniques, the adsorption process is the most widely adopted and reliable technique because of its high productivity, assessability, economic feasibility, recyclability and reuse of adsorbents and the vast choice of adsorbents^{9,17}. A large number of adsorbents have been advocated for the wastewater remediation. One of the adsorbents is activated carbon, but it is not economically desirable^{18,19}. Other alternative candidates are fly ash¹⁷, polymers¹⁹, zeolites²⁰ and clays²¹. Among all the known adsorbents, layered double hydroxides (LDHs) have been receiving consistent recognition because they offer diverse advantages such as great adsorption capacity, economically feasible and high anion-exchange properties²².

LDHs, also known as anionic clays, are extensively used in the field of catalysts and anion exchanges^{23,24}, adsorbents²⁵, anticorrosion agents²⁶, drug and catalyst carriers²⁷ and electrode materials^{28,29}. The general formula of LDH, an important inorganic layered material is $[M_{(1-x)}^{II}M_x^{III}(OH)_2]^{x+}(A^{n-})_{x/n} \cdot mH_2O$, where M^{II} and M^{III} are divalent (Cu^{2+} , Ca^{2+} , Mg^{2+} , Zn^{2+} , Ni^{2+} , Co^{2+} , etc.) and trivalent metal ions (Al^{3+} , Fe^{3+} , Ga^{3+} , Cr^{3+} , etc.), A^{n-} (Cl^- , Br^- , NO_3^- , I^- , OH^- , SO_4^{2-} , etc.) is the interlayer anion with charge n and x is the molar ratio between divalent and trivalent cations $M^{3+}/(M^{2+} + M^{3+})$ ^{29–33}. LDH materials having a wide range of physicochemical properties can be designed by various methods such as co-precipitation³⁴, ion-exchange methods³⁵, hydrothermal methods³⁶, urea hydrolysis³⁷, ultrasound irradiation³⁸ and rehydration/reconstruction³⁹. The presence of replaceable interlayer anions makes LDHs good anion-exchangers.

To enhance the adsorbent properties of LDHs, scads of variations have been introduced by the researchers across the globe, such as MgAl-LDH supported Cu-(BDC) MOF⁴⁰, Ni₄Fe₁-Cl-LDH⁴¹, ZnAl-LDH/Al(OH)₃⁴², etc (Table 1) but unfortunately they cannot be applied under high acidic or high basic conditions, exhibits toxic nature and display slow adsorption rate, thus, making them inapplicable for wastewater treatment. So, it would be of great significance to introduce a new biocompatible, environment friendly and ultrafast adsorbent for wastewater management.

Our study demonstrates the highly effective ultrafast adsorption of different organic dye contaminants over ternary Ni/Fe/Ti LDH in comparison to the previous studies^{40–46}. Here, we have reported the synthesis of a series of ternary Ni/Fe/Ti LDHs with varying Ni/Fe/Ti ratio via the hydrothermal route. The synthesized material was implemented for the dye adsorption from synthetic wastewater. The biocompatible study of synthesized Ni/Fe/Ti LDH was also carried out using MHS cell lines with varying concentrations of Ni/Fe/Ti LDH which confirmed the non-toxic behavior of synthesized rapid adsorbent and open all the channels for implementing it in water remediation.

Experimental Section

Materials. All chemicals were commercially available and were used without further purification. $Fe(NO_3)_3 \cdot 9H_2O$ and $TiCl_4$ were purchased from LOBA CHEMIA (Mumbai, India). $Ni(NO_3)_2 \cdot 6H_2O$ was purchased from THOMAS BAKER (Mumbai, India). Methyl orange, congo red, methyl blue, orange G, methylene blue and rhodamine B were purchased from SIGMA-ALDRICH (USA). HCl was purchased from FISCHER SCIENTIFIC (Mumbai, India). NaOH was purchased from spectrochem. For biocompatibility, RPMI-1640 media, trypsin, Phosphate Buffer Saline (PBS), Fetal Bovine Serum (FBS), Dimethyl Sulfoxide (DMSO), 3-(4,5-Dimethylthiazol-2-Yl)-2,5-Diphenyltetrazolium Bromide (MTT) dye were procured from himedia. MHS (Mouse macrophagic) cell line was procured from National Centre For Cell Science, Pune.

Synthesis of LDHs. Ni/Fe/Ti LDHs (NiFeTi1, NiFeTi2, NiFeTi3, NiFeTi4 and NiFeTi5) were synthesized by the hydrothermal route with varied concentrations. The synthesis was carried out by adding $Ni(NO_3)_2 \cdot 6H_2O$, $Fe(NO_3)_3 \cdot 9H_2O$, $TiCl_4$ and 1.5 g urea in 100 ml decarbonated water. The mixture was vigorously stirred and hydrothermally aged in an autoclave at 160 °C for 2 days. The product so formed was washed with distilled water and dried in an oven at 80 °C. (S2 – Electronic supplementary information)

Biocompatibility studies. MHS cell lines were grown in RPMI-1640 media in 5% CO₂ incubator at 37 °C. When the cells reached 70% confluency, they were trypsinized and harvested. Cells were counted on a

hemocytometer. 10,000 cells were seeded per well on a 96 well plate. Cells were left to attach for another 24 h. Different concentration of NiFeTi2-LDH (15 µg/ml, 31.5 µg/ml, 62.5 µg/ml and 125 µg/ml) were added to it and left for 24 h. Finally, media was pipetted out gently and 0.5 mg/ml MTT dye was added per well. After 4 h of incubation DMSO was added and left for 10 min to solubilize the formazan crystal. Absorbance was taken at 570 nm with 630 nm reference.

Characterization methods. X-ray diffractometer (Model No. D8 DISCOVER) was used to record X-ray diffraction patterns. Morphology of the synthesized material was studied using TECNAI 200 kV Transmission Electron Microscopy (TEM) (Fei, Electron Optics) and Field Emission Scanning Electron Microscope (FESEM) Model No.- ZEISS Gemini SEM-500. The Raman spectra were obtained from RenishawVia™ Reflex Micro-Raman spectrometer using 514 nm wavelength Ar⁺ laser for sample excitation. TGA spectra were recorded on LINSEIS L40/2052. FT-IR spectra were recorded on Thermo Scientific Nicolet iS 50 FTIR. UV-vis spectra were measured on Thermo Scientific Evolution 300. BET was recorded on Quantacrome Instruments Autosorb-1.

Adsorption experiments. All the adsorption experiments were performed in batches by dispersing adsorbent (20 mg) in 10 mL dye solution (20 mg/L) for 10 min (pH = actual, temperature = 25 °C). The adsorbent was further separated by centrifugation and the solution was used to evaluate the residual dye concentration by using UV-vis spectrometer. The effect of contact time, pH, amount of the adsorbent and the initial concentrations of the dye on the adsorption process were also evaluated. The adsorption kinetics was studied at time intervals of 1, 2, 4, 6, 8 and 10 min. The adsorption isotherm was studied by varying the initial dye concentrations (ranging from 10–70 mg/L).

The dye removal efficiency (DRE) was calculated by the formula:

$$\text{Dye removal efficiency (\%)} = [(C_0 - C_e)/C_0] \times 100\% \quad (1)$$

The adsorption capacity at equilibrium, q_e (mg/g) was evaluated by the equation:

$$\text{Adsorption capacity (} q_e \text{)} = (C_0 - C_e) \times V/W \quad (2)$$

The adsorption capacity at time t , q_t (mg/g) was calculated by:

$$\text{Adsorption capacity (} q_t \text{)} = (C_0 - C_t) \times V/W^3 \quad (3)$$

where, C_0 is the initial concentration of dyes, C_e is the equilibrium concentration of dyes and C_t is the concentration of dyes at respective time interval. Reaction mixture volume is denoted by V (L) and adsorbent amount used is represented by W (g).

Result and Discussion

Characterization. The XRD pattern of NiFeTi2 LDH can be easily correlated with previously reported data⁴⁷. The incorporation of CO_3^{2-} ions and H_2O molecules in the lattice of synthesized LDH can be confirmed by the 2θ values of 11.12, 22.32 and 34.31° representing (003), (006) and (009) reflections, respectively. The d-spacing of the planes (003) and (110) were found to be 0.796 nm and 0.354 nm, respectively. Due to the similarity in the basal spacing of the synthesized LDH and Ti incorporated LDHs, it could be easily stated that the interlayer CO_3^{2-} ions and H_2O molecules have retained a pattern that is similar to the previously reported XRD patterns. Moreover, the presence of (110) and (101) reflections at 25.1° and 36.5° indicates that TiO_2 exists in anatase phase in the synthesized LDH. The XRD pattern of NiFeTi2 LDH is illustrated in Fig. 1(A), XRD patterns of all the synthesized materials is depicted in Fig. S3a(A) and X-ray diffraction parameters are illustrated in Table S1.

During the variation in the prescribed synthesis of LDH, we have performed the PXRD experiment by which we came to observed that the composition of LDH is in its purest form. Simultaneously, we have observed that other material excluding NiFeTi2 LDH contains different oxides other than LDH. Therefore, we have analysed the ICP results of different as-synthesized LDH materials. The pure LDH synthesised as NiFeTi2 LDH ($\text{Ni}_{2.49}\text{Fe}_{0.2}\text{Ti}_{1.0}$) and other LDH chemical compositions, with intercalated CO_3^{2-} ions and H_2O molecules, has been provided in Table 2.

FTIR spectra of all the synthesized materials are depicted in Fig. S3a(B) and spectrum of NiFeTi2 LDH is depicted in Fig. 1(B). The broad absorption band located around 3443 cm^{-1} might be due the stretching vibration occurred because of the presence of layer's hydroxyl group and intercalated water molecules. The shoulders around 3256 cm^{-1} and 2930 cm^{-1} could be due to the H-bonding arising between the interlayer H_2O and CO_3^{2-} anions. A weaker band at 1632 cm^{-1} could be assigned to the bending vibrations of hydroxyl group. The observation band at 1387 cm^{-1} could be asymmetric stretching occurred due to the existence of carbonate ions^{48,49}.

The UV-visible spectra of all the synthesized materials are illustrated in Fig. S3a(C). The coordination state and the nature of Ni, Fe and Ti within the layered framework is introduced by the UV-vis of the various LDHs. The hump at $\approx 230\text{ nm}$, observed for all the LDHs is attributed to the d-d transitions. The strong adsorption band observed in the range of 250–460 nm can be assigned to typical metal coordinated to the CO_3^{2-} anion present in the interlayer galleries^{47,48,50–55}. A broad shoulder between 385 to 700 nm may be attributed to the existence of Ti^{4+} in the brucite-like sheets (Fig. 1(C))⁴⁷. Broad valley also signifies supramolecular guest-host interactions (hydrogen bonding, electrostatic attraction and van der Waals forces) or guest-guest interactions (van der Waals forces and hydrogen bonding).

The N_2 adsorption-desorption isotherm of NiFeTi2 is depicted in Fig. 1(D). The isotherm of NiFeTi2 LDH could be easily correlated with H-3 Type hysteresis loop. The hysteresis loop appearing at 0.6–1, suggests the presence of mesoporous material. The calculated BET surface area and Langmuir surface area were $106\text{ m}^2/\text{g}$

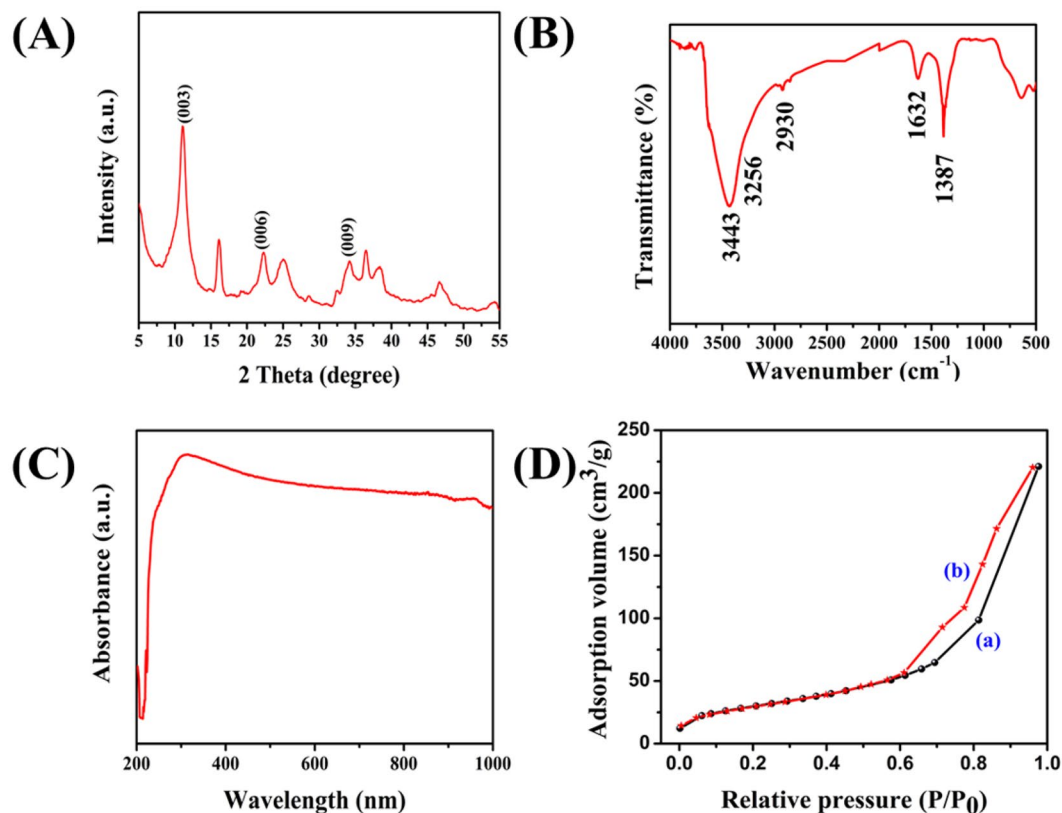


Figure 1. (A) XRD Pattern of NiFeTi2 LDH, (B) FTIR spectra of NiFeTi2 LDH, (C) UV-vis spectroscopy of NiFeTi2 LDH, (D) (a) N₂-adsorption and (b) N₂-desorption of NiFeTi2 LDH.

Dye	Pseudo-first-order			Pseudo-second-order		
	q _e (mg/g)	k ₁ (min ⁻¹)	R ²	q _e (mg/g)	k ₂ (g/mg min)	R ²
MO	8.800	0.584	0.994	10.108	0.220	0.993
CR	4.664	0.243	0.646	10.121	0.268	0.994
MB	1.359	0.432	0.452	9.798	2.934	0.999
OG	3.886	0.616	0.777	10.08	0.943	0.999

Table 2. Kinetic parameters obtained from the kinetic study.

and 1702 m²/g for NiFeTi2 LDH, respectively. The average pore diameter was also determined by using Barrett-Joyner-Halenda (BJH) method and is obtained as 10.6 nm. The BJH adsorption and desorption pore size distribution volumes were reported as 0.33 and 0.34 cm³/g, respectively^{49,56}.

In addition, SEM images (Fig. 2(c,d)) of CO₃-LDH show platelet structure. The HRTEM images (Fig. 2(a,b)) clearly indicates the sheets-like morphology of CO₃-LDH with d-spacing of 0.27 nm.

The thermogram (Fig. S3b(A)) of the synthesized materials exhibit two degradation steps. The first degradation occurs from 50–200 °C due to the elimination of surface and interlayer water, followed by second degradation (250–400 °C) due to the decarbonation and dehydroxylation (Fig. 3(A))⁴⁸.

Figures 3(B) and S3b(B) shows the Raman studies of carbonate anions in NiFeTi2 and all LDHs, respectively. In all the LDHs, ν₁ band is observed around 1038 cm⁻¹. In NiFeTi1, ν₁ is a weak band which becomes stronger in the case of NiFeTi2, which further becomes weak and broad in the case of NiFeTi3 and NiFeTi4 and finally disappears in the case of NiFeTi5. It is also observed that ν₄ band is weakest in NiFeTi1 at 628.28 cm⁻¹, stronger in NiFeTi2 at 639.1 cm⁻¹, more stronger for NiFeTi3 (639.14 cm⁻¹), broader and stronger in NiFeTi4 at 655.42 cm⁻¹ and broadest and strongest for NiFeTi5. These observed trends in ν₄ bands is due to the overlap of ν₄ band of CO₃²⁻ and M-OH of hydroxide layer as interlayer anions and this vibration is assigned to the E_g (τ) mode. These two bands overlap result in broadening of ν₄ band.

Adsorbent variation for adsorption study. Initially, MO was used to carry out the adsorption experiment aiming to select the optimum adsorbent from the series, NiFeTi1–NiFeTi5. The dye removal efficiency of each adsorbent was calculated, shown in (Fig. 4(A)). Among all adsorbents (NiFeTi1–NiFeTi5) implemented for adsorption study, the ternary NiFeTi2 which is purely LDH as compared to all other materials showed the highest

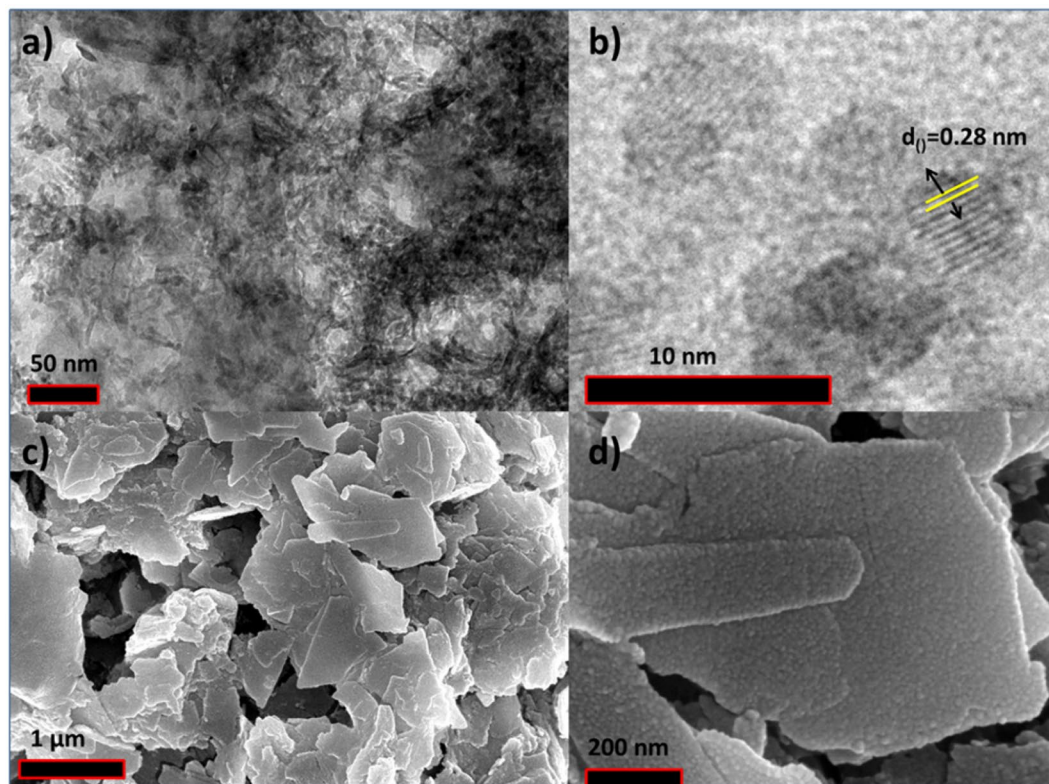


Figure 2. (a,b) HRTEM images of NiFeTi₂ LDH; (c,d) FE-SEM images of NiFeTi₂ LDH.

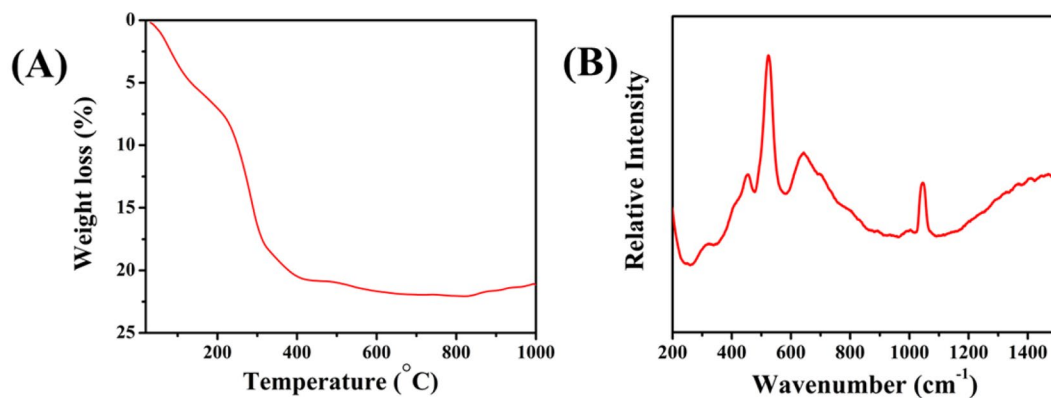


Figure 3. (A) TGA spectra of NiFeTi₂ LDH, (B) Raman spectra of NiFeTi₂ LDH.

adsorption capacity with 97.44% removal of anionic dye from aqueous solution and attained equilibrium between 4 to 6 min. This might be due to the inherent properties associated with pure LDH, mainly which are layered structure, large surface area and interlayer ion exchange⁴³. Along with this, many factors counting electronegativity, electrostatic attractions and hydrogen bonding might be responsible behind such efficient adsorption. A promising mechanism behind such adsorption could be the formation of H-bonds among the dye molecules and -OH groups of NiFeTi₂ LDH. Also, the formation of electrostatic attraction between negative and positive charges of dye molecules and NiFeTi₂ LDH surface, respectively, results in excellent adsorption of anionic dyes⁴⁸.

Dye variation for adsorption study. The adsorption studies for various organic dyes over NiFeTi₂ LDH were performed. It was observed from Fig. 5 that the anionic dyes (MO (97.44%), CR (98.63%), MB (96.81%) and OG (98.71%)) are adsorbed more preferentially over the LDH surface than cationic dyes (MeB (22.81%) and RhB (8.5%)). Moreover, the low adsorption value for cationic dyes might be because of the unfavourable resistance of positive charge present in cationic dyes from the positively charged surface of the LDH on contrary to anionic dyes. Therefore, due to the presence of opposite charge, attraction electrostatic forces took place for the adsorption of the anionic dyes and enhanced their adsorption drastically on the LDH surface. Further studies

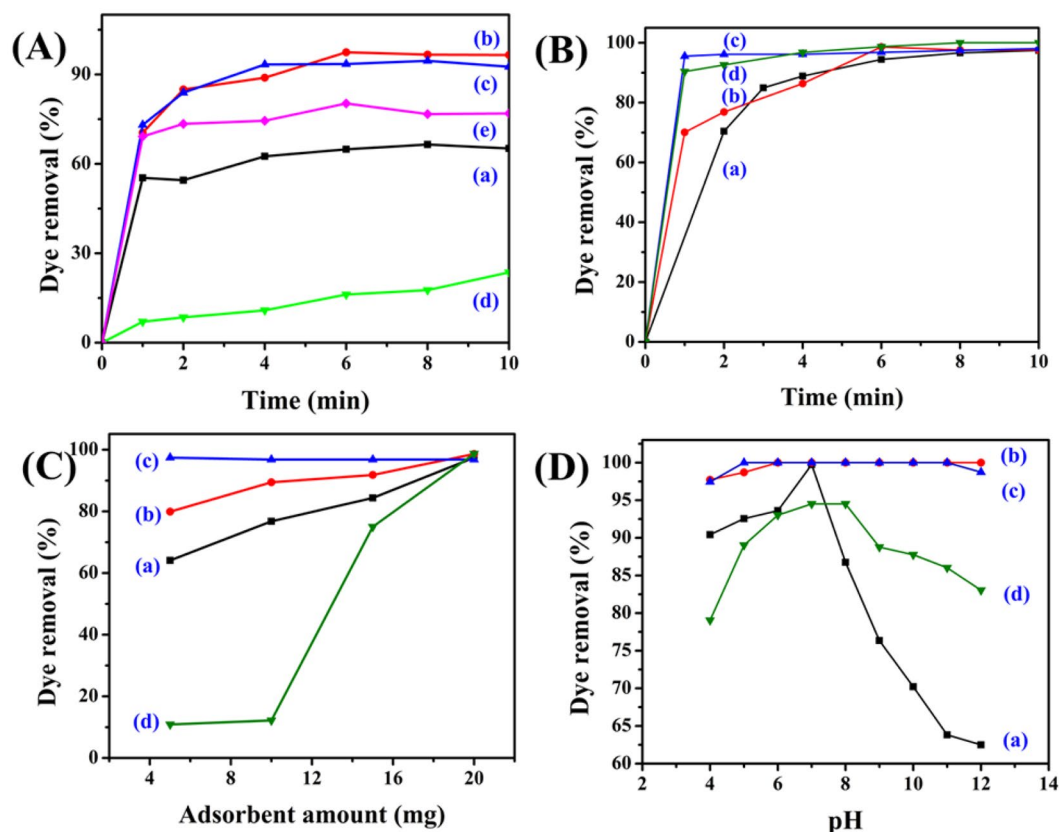


Figure 4. (A) Dye removal (%) of MO over various LDHs (Reaction conditions: adsorbent amount = 20 mg, $V_{\text{solution}} = 10$ mL, conc of MO = 20 mg/L, actual pH, temperature = 25 °C) [(a) NiFeTi1, (b) NiFeTi2, (c) NiFeTi3, (d) NiFeTi4, (e) NiFeTi5], (B) Influence of contact time over *NiFeTi2* LDH (Reaction conditions: adsorbent amount = 20 mg, dye solution = 10 mL, conc of dye solution = 20 mg/L, pH = 7.35, temperature = 25 °C) [(a) MO, (b) CR, (c) MB, (d) OG], (C) Influence of adsorbent amount over *NiFeTi2* LDH (Reaction conditions: $V_{\text{solution}} = 10$ mL, conc of dye solution = 20 mg/L, time = 10 min, pH = 7.35, temperature = 25 °C) [(a) MO, (b) CR, (c) MB, (d) OG], (D) Influence of pH on dye removal (%) of various anionic dyes over *NiFeTi2* LDH (Reaction conditions: adsorbent amount = 20 mg, $V_{\text{solution}} = 10$ mL, conc of dye solution = 20 mg/L, time = 10 min, temperature = 25 °C) [(a) MO, (b) CR, (c) MB, (d) OG].

were conducted using anionic dyes (MO, CR, MB and OG). The UV-visible spectra of time dependent adsorption of various dyes over *NiFeTi2* LDH are depicted in Fig. S4.

Effects of various parameters (contact time, adsorbent dosage, pH of the solution and initial dye concentration). The influence of contact time on dye removal (%) of MO, CR, MB and OG over *NiFeTi2* LDH is shown in Fig. 4(B). For all dyes, adsorption was achieved within 10 min from the initial start of the process which might be due to the existence of easily available active sites on the exterior surface of *NiFeTi2* LDH^{40–46}. Further, the effect of alteration in the adsorbent amount (5 to 20 mg) on the dye removal efficiency was evaluated (Fig. 4(C)). It was observed that when the amount of the adsorbent was increased the dye removal (%) also increases. Hence, from the experimental data 20 mg adsorbent amount was chosen for further evaluation.

Figure 4(D) demonstrates the cleaning efficiency of *NiFeTi2* LDH over a wide range of pH = 4 to 12 (Solutions used for adjusting pH = 0.1 M HCl, 0.1 M NaOH). The results showed that the dye removal efficiency of *NiFeTi2* LDH was highest at pH 7 (99.73% (MO), 100% (CR), 100% (MB) and 94.51% (OG)). 100% dye removal efficiency is shown by adsorbent for CR and MB at each and every pH. As per the results suggested, the effect of pH change is noteworthy and had given very indicative information for the dye and adsorbent interactions. For lower pH (pH < 7), the adsorbent is prone to the dissolution which results in adsorption and less availability of active adsorbent sites. Henceforth, dissolution of LDH at lower pH has decreased removal efficiency of dyes. According to study by Ai *et al.*, 2011, the negative charge on the adsorbent surface keeps on increasing with increase in value of pH and results in electrostatic repulsion between the anionic organic dye molecules and adsorbent surface. Therefore, in contrast to lower pH, the lower dye removal percentage at higher pH can be attributed the purely electrostatic force of repulsion¹.

Figure 6 depicts the variation in the removal efficiency of *NiFeTi2* LDH observed when the initial dye concentration was varied from 10–70 ppm. The results clearly demonstrated a gradual decrease in removal efficiency when dye concentration was increased. The dye removal efficiency decreases from 97.44 to 80.1%, 100 to 86.39%, 96.81 to 75.4% and 98.71 to 89.46%, for MO, CR, MB and OG, respectively. This change could be attributed

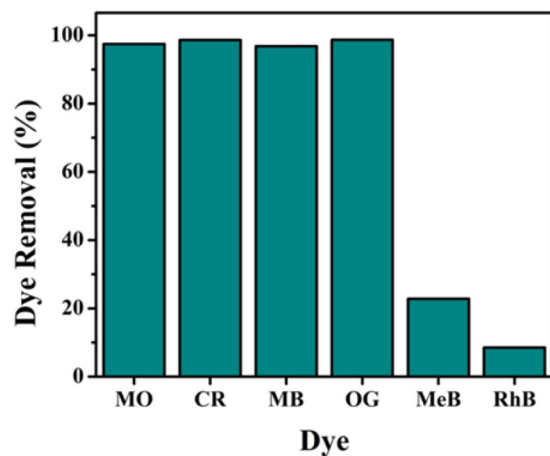


Figure 5. Removal efficiency of *NiFeTi₂ LDH* for various organic dyes (Reaction conditions: adsorbent amount = 20 mg, $V_{\text{solution}} = 10$ mL, conc of dye solution = 20 mg/L, time = 10 min, temperature = 25 °C, pH = 7.35).

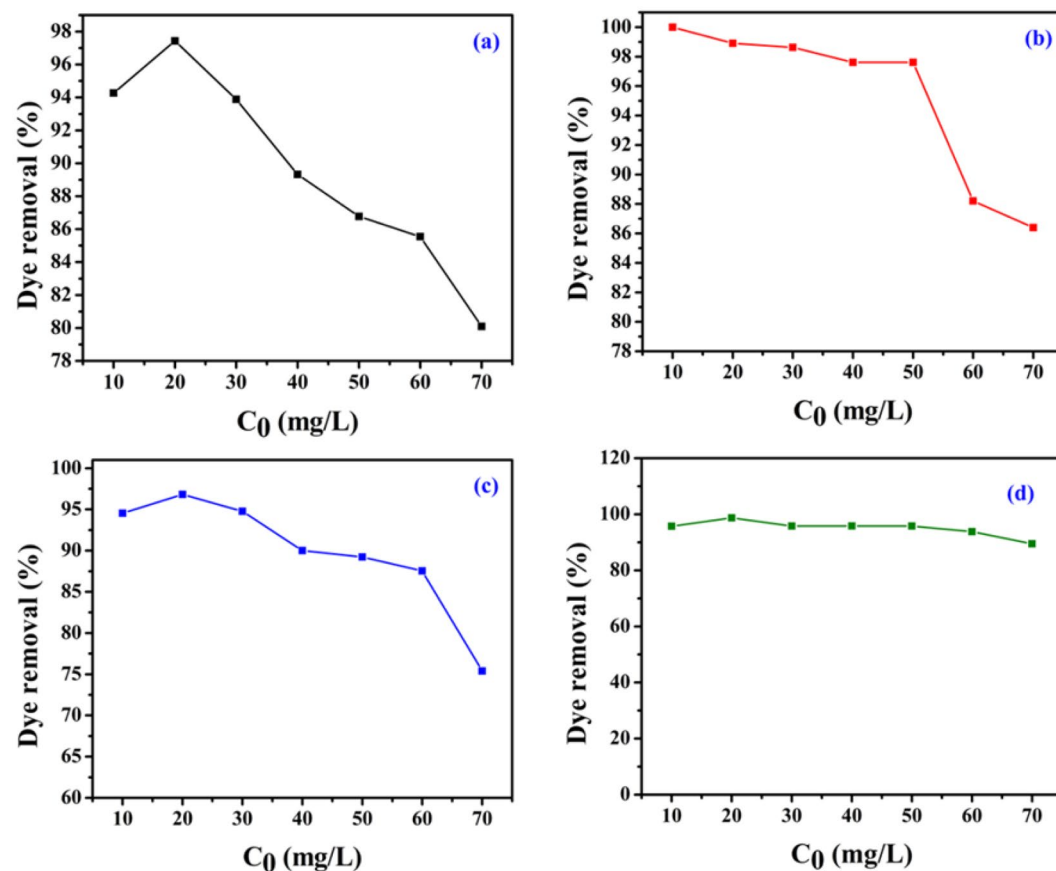


Figure 6. Dye removal (%) efficiency of *NiFeTi₂ LDH* for various initial dye concentrations dyes [(a) MO, (b) CR, (c) MB, (d) OG] ($V_{\text{solution}} = 10$ mL, adsorbent amount = 20 mg, $T = 25$ °C, Time = 10 min, pH = 7.35).

to the change in the ratio of the active adsorbent sites to the number of dye molecules with increase of dye concentration⁴⁹.

Kinetics study. Pseudo-first and second-order kinetic models are used for kinetic studies of the removal of various dyes by NiFeTi₂ LDH. The models are represented as

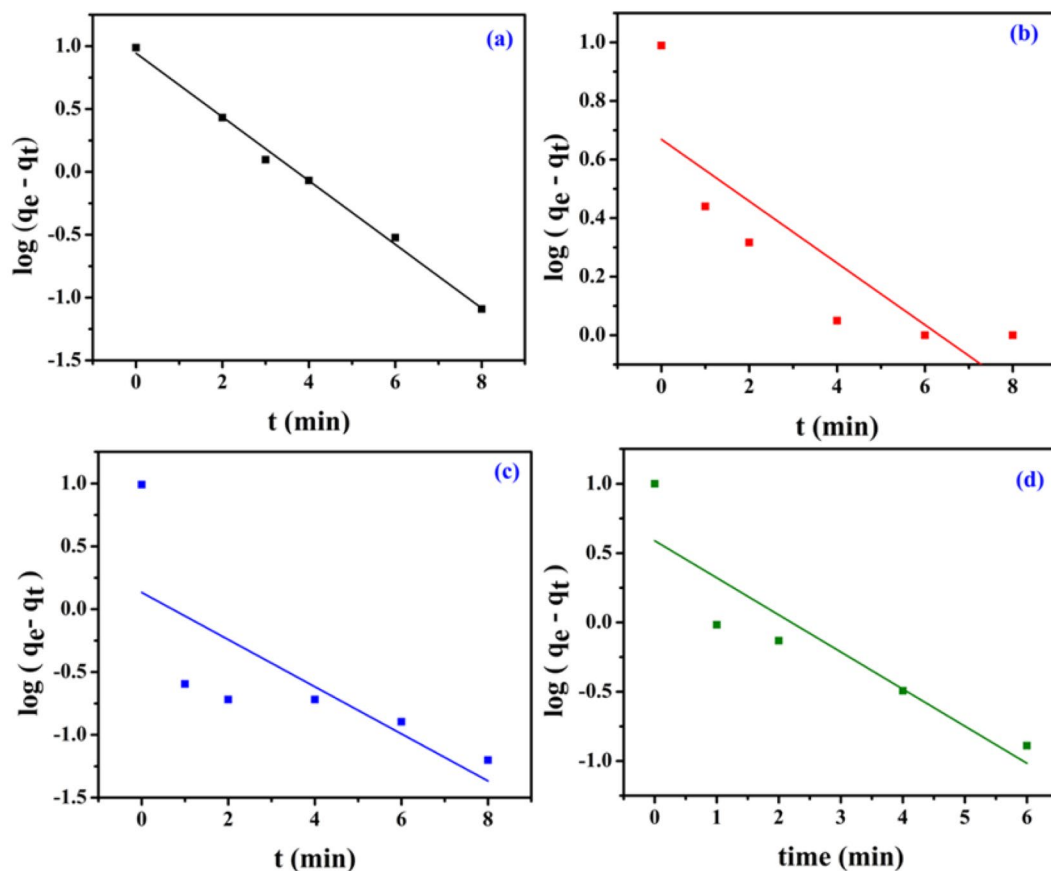


Figure 7. Kinetic plots (Pseudo-first order) for (a) MO, (b) CR, (c) MB and (d) OG adsorption ($V_{\text{solution}} = 10 \text{ mL}$, $C_0 = 20 \text{ ppm}$, adsorbent amount = 20 mg, $T = 25 \text{ }^\circ\text{C}$, $\text{pH} = 7.35$).

$$\log(q_e - q_t) = \log q_e - \frac{k_1}{2.303} t \quad (4)$$

$$\frac{t}{q_t} = \frac{1}{k_2 q_e^2} + \frac{1}{q_e} t \quad (5)$$

$$q_t = k_i t^{0.5} + C \quad (6)$$

where, q_e (mg/g) and q_t (mg/g) are the amount of dye adsorbed at equilibrium and at time (t), respectively; k_1 (min^{-1}), k_2 ($\text{g}/\text{mg min}$) and k_i ($\text{g}/\text{mg min}^{0.5}$) are the pseudo-first-order, pseudo-second-order and intraparticle diffusion rate constants, respectively and C is the intercept. The pseudo-first-order and the pseudo-second-order kinetic model fittings are illustrated in (Figs 7 and 8), and their parameters q_e , k_1 and correlation coefficient (R^2) are provided in Table 2.

From the linear form of pseudo-first order kinetic model (Eq. 4), the values of k_1 and q_e were estimated from the slope and intercept of linear plots [$\log(q_e - q_t)$ versus t] (Fig. 7). Similarly, from the linear form of pseudo-second order kinetic model (Eq. 5), the values of k_2 and q_e were evaluated (Fig. 8). All the kinetics parameters are summarized in Table 2. In all the cases, it was observed that the adsorption process followed pseudo-second order kinetic model with higher correlation coefficient (R^2) value as compared to first order kinetic model.

Using the intraparticle diffusion kinetic model (Eq. 6), the diffusion mechanism of the adsorption process was investigated. The value of k_i has been calculated by using the slope and C is the intercept of the plots of q_t versus $t^{0.5}$ (Fig. 9(A)). Here, the intercept C refers to the boundary layer thickness. For all the cases, it is observed that the adsorption process has been influenced by multiple processes. From the plots, it could be inferred that along with intraparticle diffusion mechanism another mechanism could also be responsible for the process¹. The initial portion of the plot signifies the adsorption on the outer surface of NiFeTi LDH, the second portion of the graph indicates the pores adsorption (intraparticle diffusion) and the unavailability of the free adsorptive sites after reaching the equilibrium stage is indicated by the third portion of the plot^{1,49}.

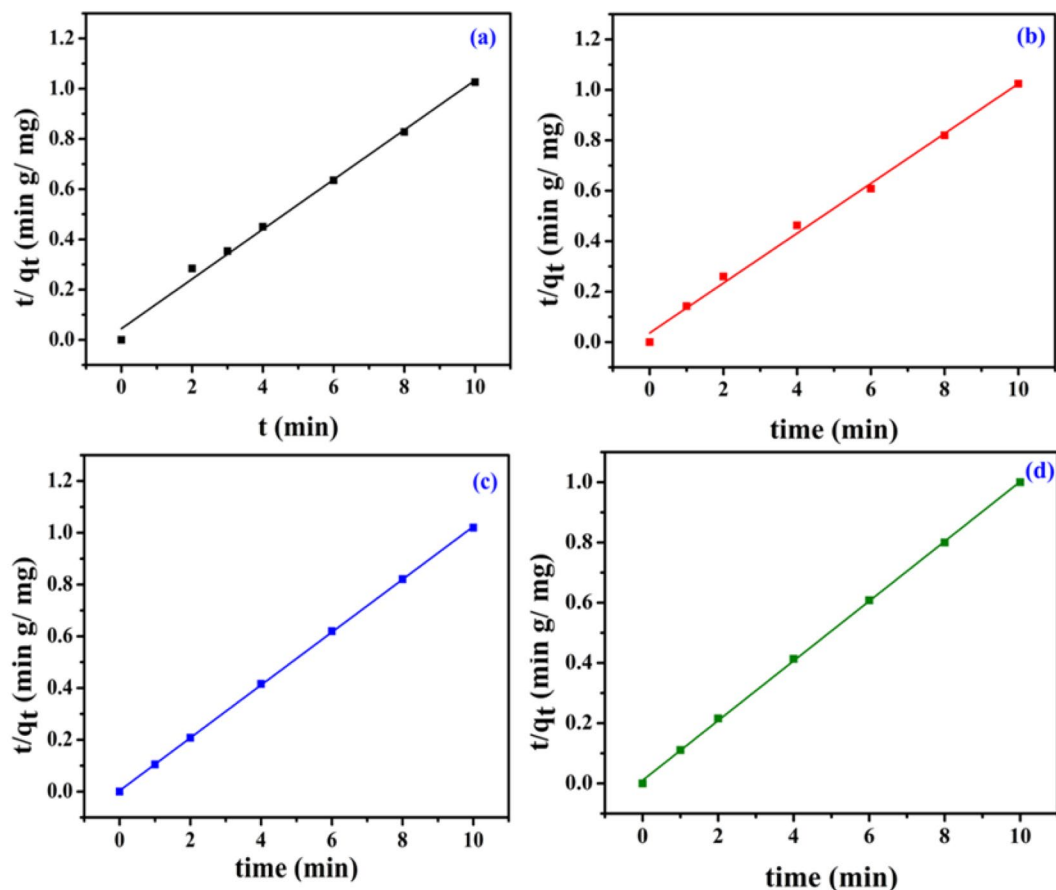


Figure 8. Kinetic plots (Pseudo-second order) for (a) MO, (b) CR, (c) MB and (d) OG adsorption ($V_{\text{solution}} = 10 \text{ mL}$, $C_0 = 20 \text{ ppm}$, adsorbent amount = 20 mg, $T = 25 \text{ }^\circ\text{C}$, $\text{pH} = 7.35$).

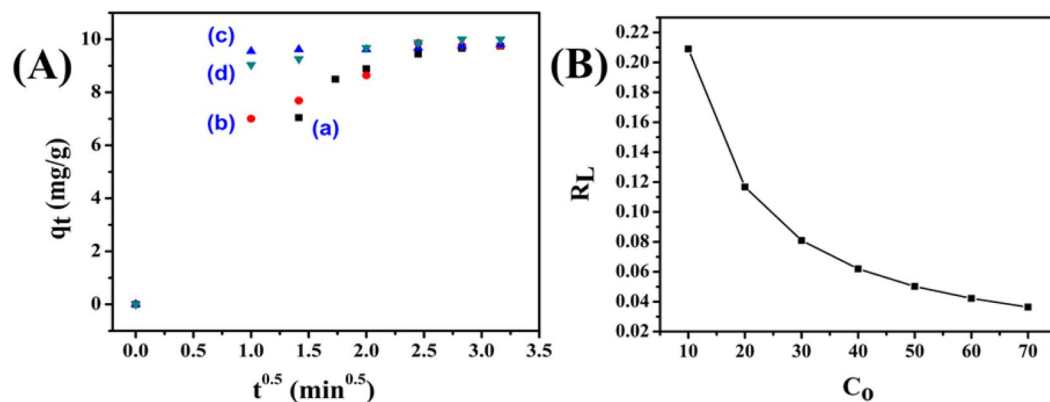


Figure 9. (A) Intraparticle diffusion kinetic plot for adsorption of (a) MO, (b) CR, (c) MB and (d) OG over NiFeTi₂ LDH ($V_{\text{solution}} = 10 \text{ mL}$, $C_0 = 20 \text{ ppm}$, adsorbent amount = 20 mg, $T = 25 \text{ }^\circ\text{C}$, $\text{pH} = 7.35$), (B) R_L v/s C_0 plot for adsorption of MO over NiFeTi₂ LDH.

Adsorption isotherm. Adsorption isotherms are the route to get qualitative information of the adsorption capacity of adsorbents and the distribution of the adsorbates between liquid and solid phases after reaching equilibrium. Langmuir and Freundlich isotherm models are used to study the adsorption capacity of the adsorbent at different equilibrium concentrations. The linear representation of the Langmuir and Freundlich isotherms are

$$\frac{C_e}{q_e} = \frac{1}{q_m b} + \frac{C_e}{q_m} \quad (7)$$

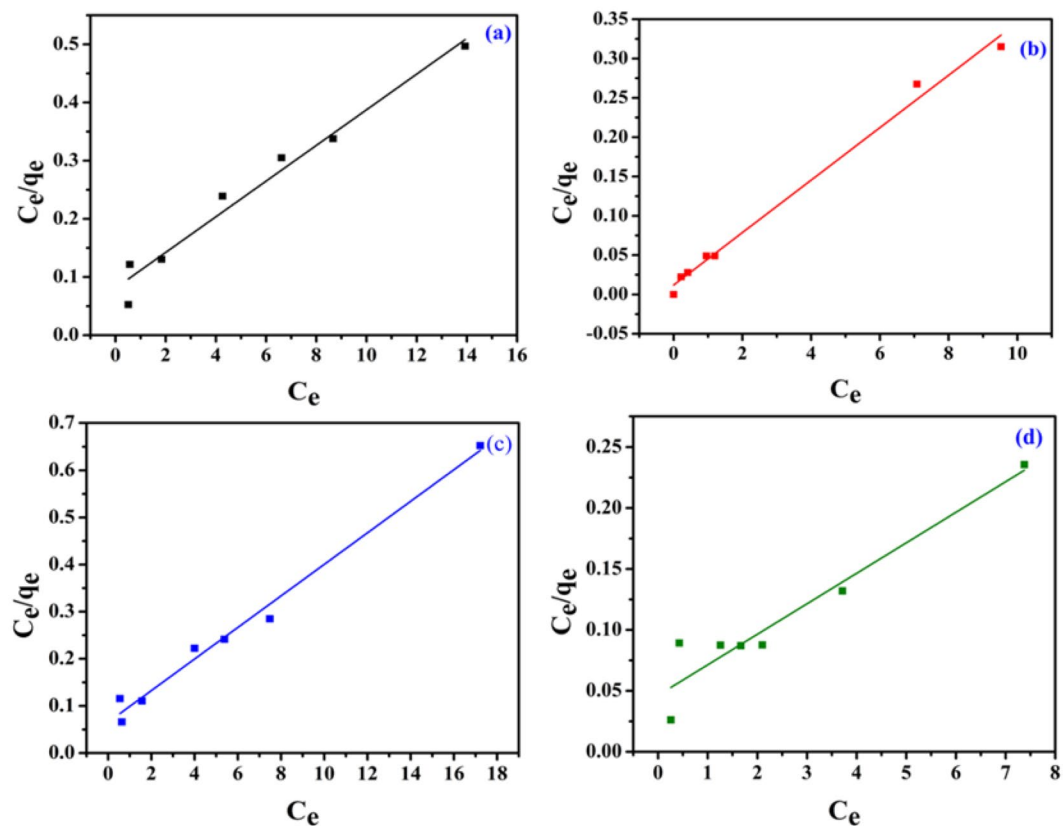


Figure 10. Isotherm plots (Langmuir model) for (a) MO, (b) CR, (c) MB and (d) OG adsorption ($V_{\text{solution}} = 10 \text{ mL}$, adsorbent amount = 20 mg, $T = 25 \text{ }^\circ\text{C}$, $\text{pH} = 7.35$).

Dye	Langmuir model			Freundlich model		
	q_m (mg/g)	b (L/mg)	R^2	K_f (mg/g) (L/mg) $^{1/n}$	n	R^2
MO	32.616	0.3785	0.967	9.379	2.24	0.832
CR	29.970	2.7898	0.991	18.00	4	0.803
MB	29.940	0.5099	0.984	9.484	2.24	0.817
OG	39.952	0.5399	0.903	13.33	2	0.734

Table 3. Isotherm parameters from isotherm study.

where, C_e (mg/L) is the equilibrium concentration of the adsorbate, q_e (mg/g) is the equilibrium adsorption capacity of the adsorbent, q_m (mg/g) is the maximum adsorption capacity of the adsorbent and b (L/mg) is the Langmuir constant. The linear plot of C_e/q_e versus C_e (Eq. 7) gives the values of q_m and b depicted in (Fig. 10) and results are summarized in Table 3. The adsorption results illustrated higher correlation coefficient (R^2) values and best fitted the Langmuir adsorption isotherm model for all the cases. The information regarding the favorability of the adsorption is determined by the dimensionless constant separation factor or equilibrium parameter, R_L , which is given by the equation,

$$R_L = \frac{1}{1 + bC_0} \quad (8)$$

where, b (L/mg) and C_0 (mg/L) are the Langmuir adsorption constant and the initial dye concentration, respectively. For an adsorption process to be favorable, the R_L value must lie between 0 and 1 ($0 < R_L < 1$). For an irreversible process, $R_L = 0$ and for an unfavorable process, $R_L > 1$. In this study, the calculated R_L values are in the range of 0 and 1 at different initial dye concentrations of various dyes which indicate that the adsorption of the dyes over NiFeTi2 LDH is a favorable process.

The linear form of the Freundlich adsorption isotherm is represented by

$$\log q_e = \frac{1}{n} \log C_e - \log k_f \quad (9)$$

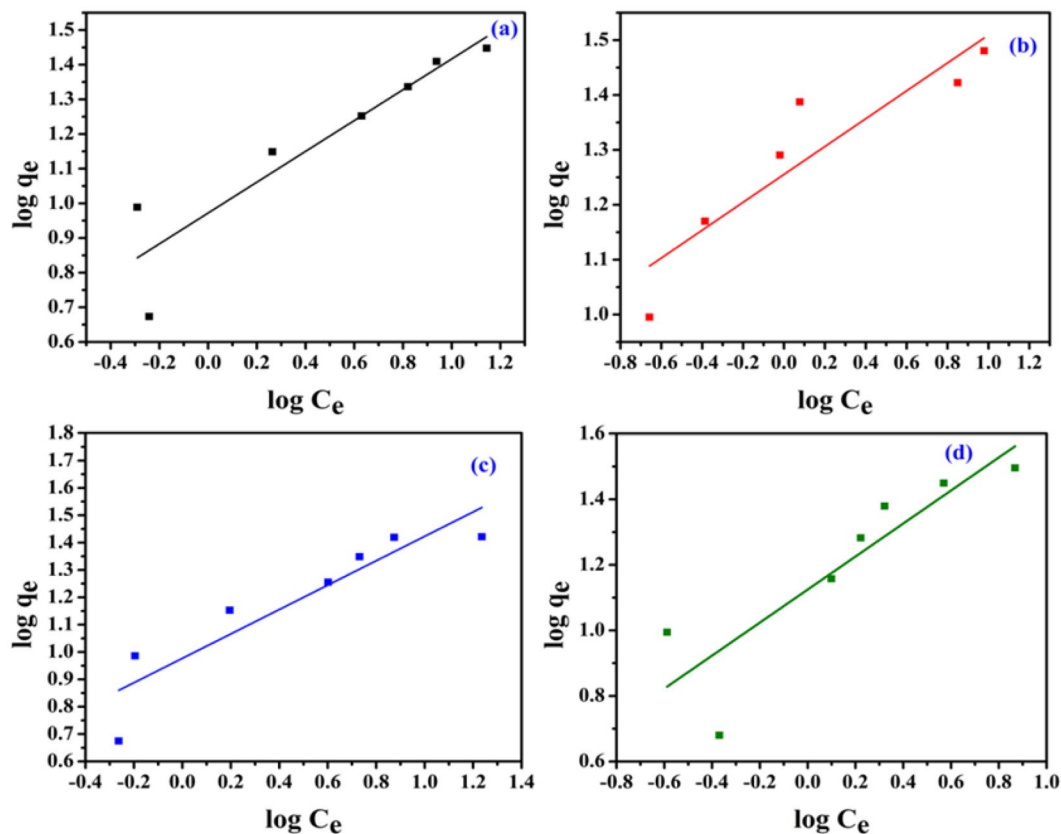


Figure 11. Isotherm plots (Freundlich model) for (a) MO, (b) CR, (c) MB and (d) OG adsorption ($V_{\text{solution}} = 10 \text{ mL}$, adsorbent amount = 20 mg, $T = 25 \text{ }^\circ\text{C}$, $\text{pH} = 7.35$).

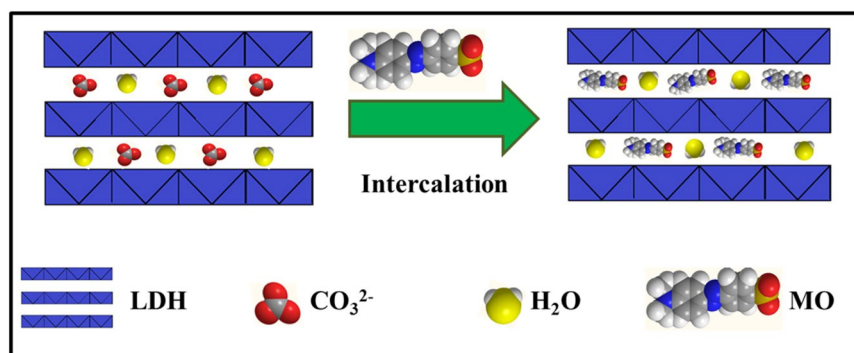


Figure 12. Schematic illustration of adsorption of MO on NiFeTi2 LDH.

where, k_f and n gives the value of the Freundlich constants. The intercept and the slope of the linear plot of $\log q_e$ versus $\log C_e$ (Fig. 11) gives us the value of k_f and n , respectively and is shown in Table 3. All the correlation coefficient (R^2) values are relatively lower than that of Langmuir isotherm. All the n values lie within 1–10, which indicates that the adsorption process is the favorable one. All the results indicate that the surface of NiFeTi2 LDH is homogeneous and follows monolayer uptake mechanism (Fig. 12).

To study the adsorption mechanism, FTIR spectra of pure NiFeTi2 LDH, MO and adsorbed MO over NiFeTi2 LDH were compared and are shown in Fig. 13(A). Creation of new bands in the case of MO adsorbed LDH in the wavenumber range of $1000\text{--}1300 \text{ cm}^{-1}$, evidences the adsorption of MO over the surface of NiFeTi2 LDH. The bands appearing around 1022 and 1120 cm^{-1} could be assigned to the vibration of the $-\text{SO}_3^-$ group and 1,4-substituent of the benzene ring of MO dye, respectively⁴⁹. The bands observed at 1176 cm^{-1} and at 1610 cm^{-1} could be attributed to the stretching vibration of C-N and C=C of the benzene ring of MO respectively. Hence, we can conclude that MO is adsorbed to the surface of NiFeTi2 LDH.

The reusability test of NiFeTi2 LDH was carried out and is illustrated in Fig. 13(B). Before carrying out the reusability test, desorption study was performed first, by suspending the used NiFeTi2 LDH in the solution of

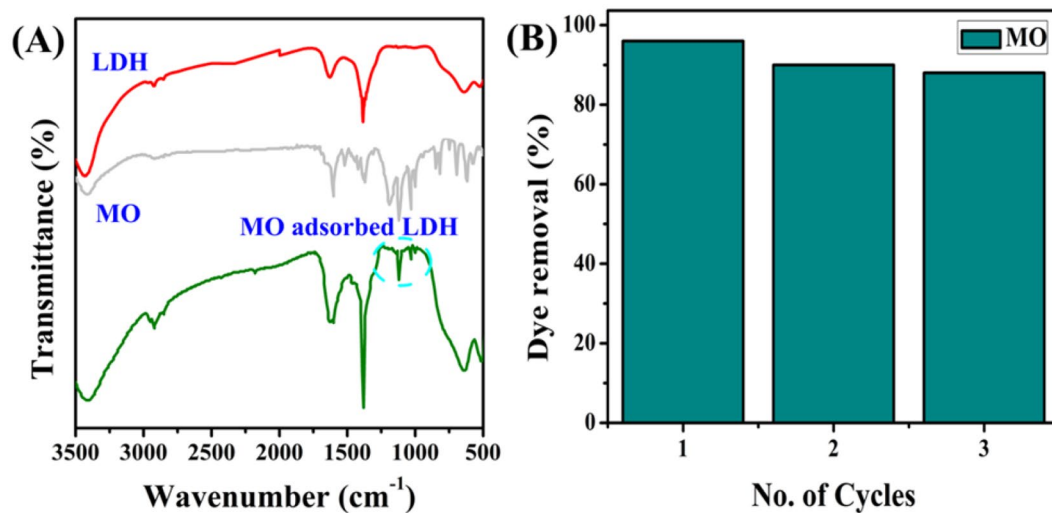


Figure 13. (A) FTIR spectra of pure NiFeTi₂ LDH, pure MO and adsorbed MO, (B) Multicyclic adsorption of MO over NiFeTi₂ LDH ($V_{\text{solution}} = 10 \text{ mL}$, $C_0 = 20 \text{ ppm}$, adsorbent amount = 20 mg, $T = 25 \text{ }^\circ\text{C}$, $\text{pH} = 7.35$).

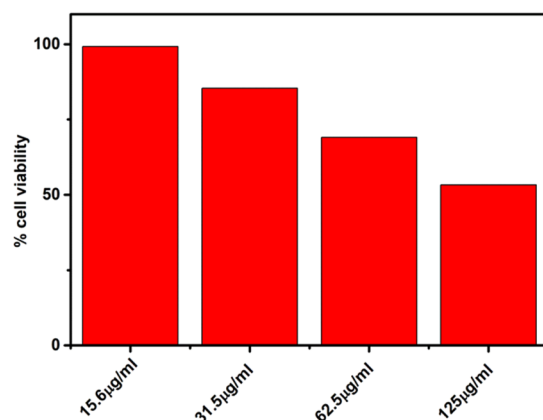


Figure 14. Biocompatibility analysis on MHS cell lines.

Na_2CO_3 and stirring it for next 24 h. After 24 h, the adsorbent was collected by centrifugation process, washed with decarbonated water and dried at $80 \text{ }^\circ\text{C}$ for 12 hours. The recovered adsorbent was again subjected for multi-cycles of adsorption for MO under similar reaction conditions. The recovered NiFeTi₂ LDH showed dye removal efficiency of 96, 90 and 88% for three successive cycles. Thus, it can be concluded that NiFeTi₂ LDH could be considered as a potential adsorbent for complete elimination of organic dyes from contaminated wastewater.

Biocompatibility. The result shows that NiFeTi LDH are biocompatible in nature. At a concentration of $15 \mu\text{g/ml}$ 100% cells are viable while on increasing the concentration the viability of cells decreases, but at a higher concentration of $125 \mu\text{g/ml}$ more than 50% cells remain viable (Fig. 14). So we can conclude that NiFeTi LDH is biocompatible in nature⁵⁶.

Conclusion

In summary, we have successfully synthesized NiFeTi LDH using the hydrothermal method and the resulting material was successfully employed in the adsorptive removal of MO, CR, MB and OG from aqueous solutions. Anionic dyes such as MO (97.44%), CR (98.63%), MB (96.81%) and OG (98.71%) showed comparatively greater adsorption than cationic dyes, MeB (22.81%) and RhB (8.5%) over NiFeTi₂ LDH at $\text{pH} = 7.35$. NiFeTi₂ gave the best dye removal efficiency (approx. 100% removal in 6 min) with greater adsorption capacity and higher kinetic rate constant. Adsorption equilibrium was attained only within 6 min at $T = 25 \text{ }^\circ\text{C}$. Pseudo-second order kinetic equation and Langmuir equation perfectly describes the adsorption equilibrium data. The dye adsorption over the LDH surface involved a physisorption process through hydrogen bonding. The reusability of the LDH for multicyclic adsorption process was also explored leading to the conclusion that NiFeTi LDH can be considered as a fast and efficient adsorbent for the removal of anionic dyes from contaminated water. The biocompatibility studies carried on MHS cell lines concluded the non-toxic behaviour of NiFeTi LDH.

Received: 27 May 2019; Accepted: 17 September 2019;

Published online: 07 November 2019

References

1. Ai, L., Zhang, C. & Meng, L. Adsorption of methyl orange from aqueous solution on hydrothermal synthesized Mg-Al layered double hydroxide. *J. Chem. Eng. Data* **56**, 4217–4225 (2011).
2. Hameed, B. H., Ahmad, A. & Aziz, N. Isotherms, Kinetics and Thermodynamics of Acid Dye Adsorption on Activated Palm. *Ash. Chem. Eng. J.* **133**, 195–203 (2007).
3. Cheng, R., Ou, S., Xiang, B., Li, Y. & Liao, Q. Equilibrium and molecular mechanism of anionic dyes adsorption on to copper (II) complex of dithiocarbamate-modified starch. *Langmuir* **26**, 752–758 (2010).
4. Munagapati, V. S. & Kim, D.-S. Adsorption of anionic azo dye Congo Red from aqueous solution by cationic modified orange peel powder. *J. Mol. Liq.* **220**, 540–548 (2016).
5. Leo, L. *et al.* Occurrence of azo food dyes and their effects on cellular inflammatory responses. *Nutrition* **46**, 36–40 (2018).
6. Oliveira, D. *et al.* A test battery for assessing the ecotoxic effects of textile dyes. *Chem. Bio. Interact.* **291**, 171–179 (2018).
7. Naveenraj, S. *et al.* A multispectroscopic and molecular docking investigation of the binding interaction between serum albumins and acid orange dye. *Spectrochimica Acta Part A: Mol. and Biomol. Spect.* **192**, 34–40 (2018).
8. Kornaros, M. & Lyberatos, G. Biological Treatment of Wastewaters from a Dye Manufacturing Company using a Trickling Filter. *J. Hazard. Mater.* **136**, 95–102 (2006).
9. Lee, J., Choi, S., Thiruvengkatachari, R., Shim, W. & Moon, H. Submerged Microfiltration Membrane Coupled with Alum Coagulation/powdered Activated Carbon Adsorption for Complete Decolorization of Reactive Dyes. *Water Res.* **40**, 435–444 (2006).
10. Selcuk, H. Decolorization and Detoxification of Textile Wastewater by Ozonation and Coagulation Processes. *Dyes Pigm.* **64**, 217–222 (2005).
11. Buonomenna, M. G., Gordano, A., Golemme, G. & Drioli, E. Preparation, Characterization and Use of PEEKWC Nanofiltration Membranes for Removal of Azur B Dye from Aqueous Media. *React. Funct. Polym.* **69**, 259–263 (2009).
12. Dutta, K., Mukhopadhyay, S., Bhattacharjee, S. & Chaudhuri, B. Chemical Oxidation of Methylene Blue using a Fenton-like Reaction. *J. Hazard. Mater.* **84**, 57–71 (2001).
13. Liu, C., Wu, J., Chiu, H., Suen, S. & Chu, K. H. Removal of Anionic Reactive Dyes from Water using Anion Exchange Membranes as Adsorbers. *Water Res.* **41**, 1491–1500 (2007).
14. Mruganandham, M. & Swaminathan, M. TiO₂–UV Photocatalytic Oxidation of Reactive Yellow 14: Effect of Operational Parameters. *J. Hazard. Mater.* **135**, 78–86 (2006).
15. Tang, H., Fu, Y., Chang, S., Xie, S. & Tang, G. Construction of Ag₃PO₄/Ag₂MoO₄ Z-scheme heterogeneous photocatalyst for the remediation of organic pollutants. *Chinese J. Catal.* **38**(2), 337–347 (2007).
16. Arami, M., Limaee, N. Y., Mahmoodi, N. M. & Tabrizi, N. S. Equilibrium and Kinetics Studies for the Adsorption of Direct and Acid Dyes from Aqueous Solution by Soy Meal Hull. *J. Hazard. Mater.* **135**, 171–179 (2006).
17. Pengthamkeerati, P., Satapanajaru, T. & Singchan, O. Sorption of Reactive Dye from Aqueous Solution on Biomass Fly Ash. *J. Hazard. Mater.* **153**, 1149–1156 (2008).
18. Bi, B., Xu, L., Xu, B. & Liu, X. Heteropoly Blue-Intercalated Layered Double Hydroxides for Cationic Dye Removal from Aqueous Media. *Appl. Clay Sci.* **54**, 242–247 (2011).
19. Ai, L., Jiang, J. & Zhang, R. Uniform Polyaniline Microspheres: A Novel Adsorbent for Dye Removal from Aqueous Solution. *Synth. Met.* **160**, 762–767 (2010).
20. Faki, A., Turan, M., Ozdemir, O. & Turan, A. Z. Analysis of Fixed-Bed Column Adsorption of Reactive Yellow 176 onto Surfactant-Modified Zeolite. *Ind. Eng. Chem. Res.* **47**, 6999–7004 (2008).
21. Ai, L., Zhou, Y. & Jiang, J. Removal of Methylene Blue from Aqueous Solution by Montmorillonite/CoFe₂O₄ Composite with Magnetic Separation Performance. *Desalination* **266**, 72–77 (2011).
22. Zhang, C., Yang, S., Chen, H., He, H. & Sun, C. Adsorption behavior and mechanism of reactive brilliant red X-3B in aqueous solution over three kinds of hydrotalcite-like LDHs. *Appl. Surf. Sci.* **301**, 329–337 (2014).
23. Vaccari, A. Preparation and Catalytic Properties of Cationic and Anionic Clays. *Catal. Today* **41**, 53–71 (1998).
24. Brito, A., Borges, M. E., Garín, M. & Hernández, A. Biodiesel Production from Waste Oil Using Mg-Al Layered Double Hydroxide Catalysts. *Energy Fuels* **23**, 2952–2958 (2009).
25. Kim, T. W., Sahimi, M. & Tsotsis, T. T. The Preparation and Characterization of Hydrotalcite Thin Films. *Ind. Eng. Chem. Res.* **48**, 5794–5801 (2009).
26. Poznyak, S. K. *et al.* Novel Inorganic Host Layered Double Hydroxides Intercalated with Guest Organic Inhibitors for Anticorrosion Applications. *ACS Appl. Mater. Interfaces* **1**, 2353–2362 (2009).
27. Panda, H. S., Srivastava, R. & Bahadur, D. *In-Vitro* Release Kinetics and Stability of Anticardiovascular Drugs Intercalated Layered Double Hydroxide Nanohybrids. *J. Phys. Chem. B* **113**, 15090–15100 (2009).
28. Li, M. *et al.* LDH Modified Electrode for Sensitive and Facile Determination of Iodate. *Appl. Clay Sci.* **46**, 396–400 (2009).
29. Ma, R., Liang, J., Liu, X. & Sasaki, T. J. General Insights into Structural Evolution of Layered Double Hydroxide: Underlying Aspects in Topochemical Transformation from Brucite to Layered Double Hydroxide. *J. Am. Chem. Soc.* **134**, 19915–19921 (2012).
30. Wang, G. *et al.* *In situ* synthesis and photoluminescence of Eu³⁺ doped Y(OH)₃@β-NaYF₄ core-shell nanotubes. *Chem. Commun.* **47**, 8019 (2011).
31. Prasad, C., Tang, H. & Liu, W. Magnetic Fe₃O₄ based layered double hydroxides (LDHs) nanocomposites (Fe₃O₄/LDHs): recent review of progress in synthesis, properties and applications. *J. Nanostructure. Chem.* **8**(4), 393–412 (2018).
32. Prasad, C., Tang, H. & Bahadur, I. Graphitic carbon nitride based ternary nanocomposites: From synthesis to their applications in photocatalysis: A recent review. *J. Mol. Liq.* (2019).
33. Prasad, C. *et al.* An overview of semiconductors/layered double hydroxides composites: Properties, synthesis, photocatalytic and photoelectrochemical applications. *J. Mol. Liq.* **289**, 111114 (2019).
34. Lopez, T. *et al.* Synthesis and Characterization of Sol–Gel Hydrotalcites Structure and Texture. *Langmuir* **12**, 189–192 (1996).
35. Morel-Desrosiers, N. *et al.* Intercalation of Dicarboxylate Anions into a Zn-Al-Cl Layered Double Hydroxide: Microcalorimetric Determination of the Enthalpies of Anion Exchange. *J. Mater. Chem.* **13**(10), 2582–2585 (2003).
36. Ogawa, M. & Asai, S. Hydrothermal Synthesis of Layered Double Hydroxide Deoxycholate Intercalation Compounds. *Chem. Mater.* **12**, 3253–3255 (2000).
37. Oh, J., Hwang, S. & Choy, J. The Effect of Synthetic Conditions on Tailoring the Size of Hydrotalcite Particles. *Solid State Ionics* **151**, 285–291 (2002).
38. Seida, Y., Nakano, Y. & Nakamura, Y. Crystallization of Layered Double Hydroxides by Ultrasound and the Effect of Crystal Quality on their Surface Properties. *Clay Clay Miner.* **50**, 525–532 (2002).
39. Erickson, K. L., Bostrom, T. E. & Frost, R. L. A Study of Structural Memory Effects in Synthetic Hydrotalcites using Environmental SEM. *Mater. Lett.* **59**, 226–229 (2005).
40. Chakraborty, A. & Himadri, A. Facile Synthesis of MgAl-Layered Double Hydroxide Supported Metal Organic Framework Nanocomposite for Adsorptive Removal of Methyl Orange Dye. *Colloid and Interface Science Communications* **24**, 35–39 (2018).

41. Jiemei, G. *et al.* Efficient Removal of Methyl Orange and Heavy Metal Ion from Aqueous Solution by NiFe-Cl-Layered Double Hydroxide. *Environ. Eng. Sci.* **35**, 373–381 (2018).
42. Xingzhong, G., Yin, P. & Yang, H. Superb adsorption of organic dyes from aqueous solution on hierarchically porous composites constructed by ZnAl-LDH/Al (OH) 3 nanosheets. *Micropor. Mesopor. Mat.* **259**, 123–133 (2018).
43. Mukarram, Z. *et al.* Starch-NiFe-layered double hydroxide composites: Efficient removal of methyl orange from aqueous phase. *J. Mol. Liq.* **249**, 254–264 (2018).
44. Qingfeng, Y., Wang, S., Shi, W., Lu, C. & Liu, G. Graphene quantum dots in two dimensional confined and hydrophobic space for enhanced adsorption of nonionic organic adsorbates. *Ind. Eng. Chem. Res.* **56**, 583–590 (2017).
45. Miandad, R. *et al.* Untapped conversion of plastic waste char into carbon-metal LDOs for the adsorption of Congo red. *J. Colloid Interface Sci.* **511**, 402–410 (2018).
46. Zhang, H. *et al.* Superadsorption capability of rhombic dodecahedral Ca-Al layered double oxides for Congo red removal. *J. Alloys Comp.* **768**, 572–581 (2018).
47. Chowdhury, P. R. & Bhattacharyya, K. G. Ni/Co/Ti layered double hydroxide for highly efficient photocatalytic degradation of Rhodamine B and Acid Red G: a comparative study. *Photochem. & Photobiol. Sc.* **16**(6), 835–839 (2017).
48. Zhang, M., Yao, Q., Lu, C., Li, Z. & Wang, W. Layered double hydroxide-carbon dot composite: high-performance adsorbent for removal of anionic organic dye. *ACS appl. materials & interfaces* **6**(22), 20225–20233 (2014).
49. Bharali, D. & Deka, R. C. Preferential adsorption of various anionic and cationic dyes from aqueous solution over ternary CuMgAl layered double hydroxide. *Coll. and Surf. A: Physicochem. and Eng. Asp.* **525**, 64–76 (2017).
50. Malik, R., Ramteke, D. S. & Wate, S. R. Physico-chemical and surface characterization of adsorbent prepared from groundnut shell by ZnCl₂ activation and its ability to adsorb colour. *Indian J. Chem. Technol.* **13**, 319–328 (2006).
51. He, J. *et al.* Preparation of layered double hydroxides *Struct. Bond. Springer-Verlag (Berlin)* **119**, 89 (2006).
52. Mohapatra, L. & Parida, K. M. Dramatic activities of vanadate intercalated bismuth doped LDH for solar light photocatalysis. *Phys. Chem. Chem. Phys.* **16**, 16985 (2014).
53. Wang, C. J. *et al.* Reverse Micelle Synthesis of Co-Al LDHs: Control of Particle Size and Magnetic Properties. *Chem. Mater.* **23**, 171–180 (2011).
54. Yang, M. Q., Zhang, N., Pagliaro, M. & Xu, Y. J. Artificial photosynthesis over graphene-semiconductor composites. Are we getting better? *Chem. Soc. Rev.* **43**, 8240 (2014).
55. Zhang, Y., Tang, Z. R., Fu, X. & Xu, Y. J. TiO₂-graphene nanocomposites for gas-phase photocatalytic degradation of volatile aromatic pollutant: is TiO₂-graphene truly different from other TiO₂-carbon composite materials? *ACS Nano* **4**, 7303 (2010).
56. Bagbi, Y., Saraswat, A., Mohan, D., Pandey, A. & Solanki, P. R. Lead and Chromium Adsorption from Water using L-Cysteine Functionalized Magnetite (Fe₃O₄) Nanoparticles. *Sci. rep.* **7**(1), 7672 (2017).

Acknowledgements

Garima Rathee is highly grateful and thankful to the University of Delhi and SERB (DST) for providing financial support to carry out our research work.

Author contributions

G.R. designed and performed the experiments; G.R., A.A. and D.S. analyzed the data; G.R., A.A., D.S., R.T. and V.T. prepared the tables and figures. G.R. and R.C. revised and reviewed the manuscript.

Competing interests

The authors declare no competing interests.

Additional information

Supplementary information is available this paper at <https://doi.org/10.1038/s41598-019-52849-4>.

Correspondence and requests for materials should be addressed to R.C.

Reprints and permissions information is available at www.nature.com/reprints.

Publisher's note Springer Nature remains neutral with regard to jurisdictional claims in published maps and institutional affiliations.



Open Access This article is licensed under a Creative Commons Attribution 4.0 International License, which permits use, sharing, adaptation, distribution and reproduction in any medium or format, as long as you give appropriate credit to the original author(s) and the source, provide a link to the Creative Commons license, and indicate if changes were made. The images or other third party material in this article are included in the article's Creative Commons license, unless indicated otherwise in a credit line to the material. If material is not included in the article's Creative Commons license and your intended use is not permitted by statutory regulation or exceeds the permitted use, you will need to obtain permission directly from the copyright holder. To view a copy of this license, visit <http://creativecommons.org/licenses/by/4.0/>.

© The Author(s) 2019